Journal of Materials Science & Technology 108 (2022) 82–89

Contents lists available at ScienceDirect

Journal of Materials Science & Technology

journal homepage: www.elsevier.com/locate/jmst

Significantly enhanced varistor properties of $CaCu_3Ti_4O_{12}$ based ceramics by designing superior grain boundary: Deepening and broadening interface states

Zhuang Tang[a,b], Kai Ning[a], Zhiyao Fu[a], Ze Lian[c], Kangning Wu[d,*], Shoudao Huang[b]

[a] State Key Laboratory of Disaster Prevention and Reduction for Power Grid Transmission and Distribution Equipment, SGCC (State Grid Corporation of China), Changsha 410000, China
[b] College of Electrical and Information Engineering, Hunan University, Changsha 410082, China
[c] State Grid Shanxi Electric Power Research Institute, Taiyuan 030001, China
[d] State Key Laboratory of Electrical Insulation and Power Equipment, Xi'an Jiaotong University, Xi'an 710049, China

ARTICLE INFO

Article history:
Received 26 May 2021
Revised 29 July 2021
Accepted 30 July 2021
Available online 29 October 2021

Keywords:
Schottky barrier
Grain boundary
Varistor ceramics
Interface states

ABSTRACT

Significantly enhanced varistor properties via tailoring interface states were obtained in $Ca_{1-2x/3}$YxCu3Ti4O12-SrCu3Ti4O12 composite ceramics. The breakdown field was improved to 35.8 kV•cm^{-1} and the nonlinear coefficient in 0.1–1 mA cm^{-2} was enhanced to 14.6 for $Ca_{0.67}Y_{0.5}Cu_3Ti_4O_{12}$-$SrCu_3Ti_4O_{12}$. Noticeably, the withstand voltage of single grain boundary reached up to 24 V while the reported ones were constant to about 3 V. Greatly improved properties were attributed to the formation of superior grain boundary rather than the reduced grain size. Surprisingly, with distinct discrepancy of nonlinear performance in the composites, the resistance and activation energy of grain boundary exhibited little differences. Based on the double Schottky barrier at grain boundary and the field-assisted thermal emission model, it was found that the excellent electrical nonlinearity arose from the formation of deeper and broader interface states at grain boundary. In this case, interface states were not easily entirely filled and the barrier could maintain its height under applied voltage. This work provides a novel routine for enhancing the varistor properties of $CaCu_3Ti_4O_{12}$ based ceramics by manipulating interface states at grain boundary.

1. Introduction

The demand for device miniaturization, integration and multi-function has become a critical goal in the current research of electroceramics, due to the rapid development of new energy industry, information technology and artificial intelligence [1–3]. $CaCu_3Ti_4O_{12}$ (CCTO), which has stable colossal permittivity (CP, $>10^3$) in a wide frequency and temperature range (10–10^6 Hz, 100–400 K), is considered as a potential lead-free candidate for application of high-integrated devices [4–8]. In addition, distinct nonlinear current-voltage characteristics are also detected in CCTO ceramics [9,10]. The above outstanding properties make it possible to be a novel dual-function capacitor-varistor material and play a key role in active areas of protecting devices against voltage transient surges and noises, memory devices and high-voltage capacitive devices [11–13].

However, relatively low breakdown field, low nonlinear coefficient and high dielectric loss are the existing challenges for practical application of CCTO-based ceramics. Generally, breakdown field and nonlinear coefficient (in the range of 0.1–1 mA cm^{-2}) of CCTO ceramics are between 1 and 2 kV cm^{-1} [14,15] and 4–6 [16,17], respectively, which heavily restrict its application in varistor areas. Moreover, dielectric loss of more than 0.1 would generate severe heat-emitting, greatly deteriorating efficiency and resulting in device failure. To solve these problems, researchers have made great efforts in property-optimizing through preparation adjustment [18–21], element-doping [16,22–25] and composite ceramics [12,26,27]. Compared to other methods tailoring varistor properties, it is illustrated that CCTO composites demonstrate significantly enhanced varistor properties, as shown in Fig. 1. In CCTO composites, the breakdown field exceeding 10 kV cm^{-1}, nonlinear coefficient more than 10 and CP with reduced dielectric loss are obtained, exhibiting its superiority in optimizing CCTO based ceramics.

In terms of microstructure analysis, grain boundary (GB) is generally accepted fundamental on determining the electrical prop-

* Corresponding author.
E-mail address: wukning@xjtu.edu.cn (K. Wu).

https://doi.org/10.1016/j.jmst.2021.07.057
1005-0302/

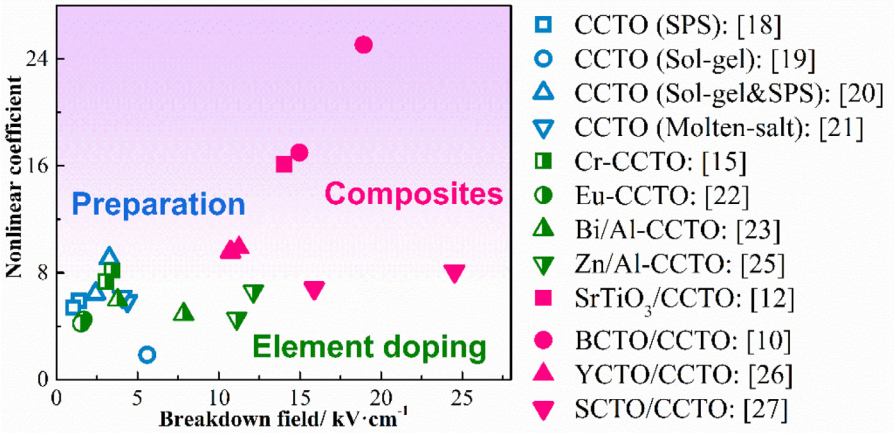

Fig. 1. Nonlinear coefficient and breakdown field in reports of CCTO based ceramics.

erties of CCTO based ceramics. On one hand, colossal permittivity of CCTO ceramics was ascribed to electrical inhomogeneity between grain and GB, which was also known as internal barrier layer capacitor (IBLC) [28]. On the other hand, existence of Schottky-type GB was confirmed [29] and the varistor properties of CCTO ceramics were further correlated with electron trapping of both point defects in depletion layers and interface states of Schottky barrier [30]. Therefore, both the capacitor and varistor properties of CCTO based ceramics are closely related with GB performance so that it is, in theory, an effective method to optimize nonlinear and dielectric properties through tailoring GB. Practically, in our previous work, varistor properties was significantly enhanced via CCTO-ACTO (Y2/3Cu3Ti4O12 [26], SrCu3Ti4O12 [31], Bi2/3Cu3Ti4O12 [12]) composites systems, which was attributed to successfully modified GB. However, GB performance was commonly studied through impedance spectra and capacitor-voltage characteristics by calculating the static parameters. Dynamics of GB, especially the evolution of defect structures at Schottky barrier, were seldom reported. In addition, improved properties of CCTO based ceramic were related with decreased grain size in a certain extent, while performance of single GB was only slightly enhanced (shown in Section 3.3 in detail). Since points defect evolution and interface states influencing on electrical properties remain unclear, manipulating GB performance and optimizing capacitor-varistor properties of CCTO based ceramics on the defect level are still challenging problems.

Among CCTO-ACTO composites, CCTO-SCTO composites exhibit superior dielectric and nonlinear properties, as shown in Fig. 1. The breakdown field can be greatly elevated to 24.52 kV cm^{-1} which is an extremely enhancement in CCTO based ceramics and nonlinear coefficient at current range of 0.1–1 mA cm^{-2} can be increased to 8.11 [27]. In addition, since the valence electron configuration of Sr and Ca are similar, Sr^{2+} substitution for Ca^{2+} maintains the electronic structure and the variation of nonlinear and dielectric properties can exclude the possibility of intrinsic polarizations. Thus, the analysis of performance variation can be focused on extrinsic relaxations which originated from GB area.

From all above, it can be concluded that the GB is the key for the optimized varistor-capacitor properties of CCTO based ceramics and composites system is a potential way to tailor the GB by introducing heterogeneous interfaces. Nevertheless, the mechanism of how the inhomogeneous interface influences the GB area remains ambiguous and needs to be further studied. In this work, the depletion layer and GB area are simultaneously manipulated by introducing both Y3+ donor and SrCu3Ti4O12 secondary phase. The heterogenous structure is distinguished by microstructure analysis and optimized dielectric and varistor properties are acquired. Based on the double Schottky barrier model and the field-assistant thermal emission model, the capability and energy level distribution of interface states are systematically studied and the relation between interface state and varistor properties is explored in depth.

2. Experiment procedure

$0.5Ca_{1-2x/3}YxCu3Ti4O12^{-}0.5SCTO$ (x = 0, 0.1, 0.5, 0.9) composites were prepared by traditional solid state reaction method. Analytical grade of $CaCO_3$ (99%), Y_2O_3 (99%), $SrCO_3$ (99%), CuO (99%), TiO_2 (99%) were selected as raw materials. Initially, powders of $Ca_{1-2x/3}YxCu3Ti4O12$ and SCTO were ball-milled in grinding machine and calcined in air at 950 °C for 15 h, respectively. After calcination, powders of $Ca_{1-2x/3}YxCu3Ti4O12$ and SCTO were mixed together by molar ratio of 1:1. Then the mixed powders were ball-milled again and granulated with adding 2 wt% of polyvinyl alcohol (PVA) as binder. Afterward, the composite powders were pressed into green pellets of 15 mm in diameter and 2.5 mm in thickness under 100 MPa. Eventually, after PVA was removed at 450 °C, the pre-sintered pellets were sintered in air at 1000 °C for 5 h and furnace cooled to room temperature. The $0.5Ca_{1-2x/3}YxCu3Ti4O12$–0.5SCTO ($x$ = 0, 0.1, 0.5, 0.9) composites were labeled as CCTO-SCTO, 0.1YCCTO-SCTO, 0.5YCCTO-SCTO and 0.9YCCTO-SCTO, respectively.

The density of the composite samples was measured through the Archimedes method by a densimeter (Etnaln, ET-120S, China). Phase composition of the composites was examined by X-ray diffraction (XRD, Regaku Smartlab-SE, Japan) technology over the 2θ ranges of 10−80 ° Surface morphology and element distribution were observed by field emission scanning electron microscopy (FE-SEM, Regulus 8100, Japan) equipped with energy-dispersive X-ray spectrometry (EDS).

In order to accomplish electrical and dielectric measurement, the pellets were polished and sputtered with Au by a sputter coating unit (Quorum Q150T, UK). The current-voltage (I-V) behavior at room temperature was characterized by an automatic test system (Haiwo HVVA-20, China). The breakdown field E_b is defined as:

$$E_b = U_{1mA}/t \quad (1)$$

where U_{1mA} is the voltage at 1 mA cm^{-1} and t is thickness of the sample. The nonlinear coefficient α is calculated as:

$$\alpha = \ln(I_1/I_2)/\ln(U_1/U_2) \quad (2)$$

where I_1 and I_2 are current density of sample and U_1 and U_2 are voltages at I_1 and I_2, respectively. In this paper, the current density range of I-V measurement was between 0.1−1 mA

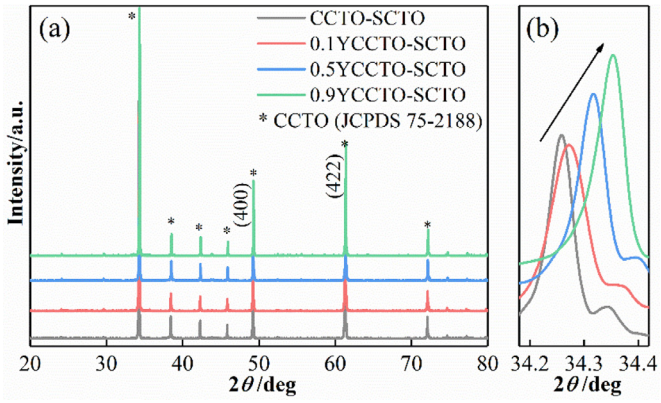

Fig. 2. XRD patterns (a) and the enlarged view of the (220) peak (b) of the composite samples.

Table 1
Lattice constant (a), theoretical density (ρ_{th}), experimental density (ρ_{ex}), and relative density (ρ_r) of the YCCTO-SCTO composite samples.

Samples	a (Å)	ρ_{th} (g cm^{-3})	ρ_{ex} (g cm^{-3})	ρ_r (%)
CCTO-SCTO	7.4030	5.21	4.77	91.6
0.1YCCTO-SCTO	7.4024	5.23	5.02	96.0
0.5YCCTO-SCTO	7.3974	5.26	4.76	90.5
0.9YCCTO-SCTO	7.3966	5.29	4.53	85.6

cm^{-1}. The capacitance-voltage (C-V) measurements and frequency-/temperature-dependent dielectric properties of the composites were obtained by an impedance analyzer (Novocontrol Concept 80, Germany). The frequency and temperature range of the measurement were 10^{-1}–10^7 Hz and 140–200 °C, respectively.

3. Results and discussion

3.1. Phase composition and microstructure

The XRD patterns of the composite ceramic samples are shown in Fig. 2. All the samples present only one perovskite phase, which is detected as CCTO phase (JCPDS 75-2188). Cu-rich phase, which is closely correlated with abnormal grain growth, is not identified in these samples. In addition, enlarged XRD patterns focusing on diffraction peak (220) are given in Fig. 2(b). With higher concentration of Y doping in CCTO, the diffraction peak (220) moves to higher angle from 34.26 to 34.35 ° According to the Bragg equation, the results support that Y substitutes Ca/Sr at A site as ionic radius of Y^{3+} (90 pm) is smaller than that of Ca^{2+}/Sr^{2+} (100/118 pm) [32,33]. The lattice constants of samples are also calculated from XRD patterns and listed in Table 1. It is reversely proportional to Y content because the crystal cell shrinks when Ca^{2+}/Sr^{2+} ions are replaced by smaller Y^{3+} ions. Relative densities of the samples were measured by the Archimedes method and listed in Table 1, as well. Dense ceramic bodies are formed for all the samples. The relative density reaches its maximum of 96.0% at 0.1YCCTO-SCTO while abundant Y doping could deteriorate the dense structure of YCCTO-SCTO composites.

The micro-morphology of polished composite ceramic samples is shown in Fig. 3. Apparently, in all the samples, majority of grains are exhibited as rectangle-shape while a few smaller sphere-shape grains can be found as well. The grain size distributions characterized by linear interception technique are plotted in Fig. S1 in supplementary material. CCTO-SCTO composites without Y doping shows the smallest average grain size of 3.48 μm while average grain size of YCCTO-SCTO composites significantly raises to more than 6 μm. Moreover, the average grain size slightly increased from 6.39 to 7.08 μm with higher Y doping content. It indicates that addition of Y promotes grain growth of CCTO-SCTO composite system.

Element distributions at the typical regions in Fig. 3 are further measured by EDS and listed in Table 2. The distribution of element can be categorized into 3 types: the interior of the grains is Ca-rich at A site, labeled as Ca-Grain (Ca-G) region; the periphery of the grains is Sr-rich at A site, labeled as Sr-Grain (Sr-G) region; the small sphere-shape grains in the intergranular region of the rectangle grains, labeled as Grain-Boundary (GB) region. In Ca-G region, it is evident that Sr can be hardly detected and Y is in relatively low ratio as well. In contrast, in Sr-G region and GB region, ratio of Sr and Y increases remarkably while ration of Ca drops sharply. Noticeably, in GB region, the weight ration of Sr maintains more than 40% and Y raises from 4.11 to 20.90% with increasing Y doping content, which indicates that Y segregates with Sr at GB region. Besides, the discrepancy between Ca-G and Sr-G region suggests a core-shell structure where Ca-G region stands for the core section and Sr-G region for the shell section. Since the narrow location of Sr^{2+} at A site, the deficiency of Sr site could result in the diffusion of Sr towards external section of grains during sintering process, contributing in the Sr rich area at shell section [34].

3.2. Nonlinear current-voltage characteristics and dielectric performance

Fig. 4(a) shows the electric field (E)-current density (J) characteristics of the composite ceramic samples. Distinct electrical nonlinearity is observed in all the samples and the relevant parameters are further calculated and listed in Table 3. Remarkably, breakdown fields E_b of all the samples are more than 20 kV cm^{-1}, which is a huge and stable improvement compare to recent reports. The addition of Y content trends to further enhance the breakdown field. Compared to 25.34 kV cm^{-1} of CCTO-SCTO, E_b reached up to 32.36 kV cm^{-1} for 0.1YCCTO-SCTO and 35.82 kV cm^{-1} for 0.5YCCTO-SCTO. Similar phenomenon happens to nonlinear coefficient αin the current range of 0.1∼1 mA cm^{-2}. Its maximum is 14.65 for 0.5YCCTO-SCTO and all the samples exhibit distinct nonlinear property of α more than 7.

Frequency-dependent permittivity ε' and dielectric loss tanδ of the composites at room temperature are presented in Fig. 4(b). Apparently, all the samples maintain colossal permittivity. In CCTO-based ceramics, the permittivity is generally contributed by three processes, high frequency process (I), mid-range frequency process (II) and low frequency process (III). Permittivity reduces from CCTO-SCTO to 0.5 YCCTO-SCTO and then rise at 0.9YCCTO-SCTO, which corresponds to promotion of process I/III and suppression of process II with increasing Y doping concentration. As process III stands for electron transportation at grain boundary, low Y content could inhibit the conduction process effectively to distinctly reduce the dielectric loss at low frequency. Hence, the minimum dielectric loss was suppressed to 0.036 at 7 Hz for 0.1YCCTO-SCTO composite and 0.038 at 10 Hz for 0.5YCCTO-SCTO and dielectric loss of 50 Hz is reduced to around 0.05, showing potential prospects applied in power industry.

3.3. Significantly enhanced properties of grain boundary

Both the dielectric properties and electrical nonlinearity are closely correlated with the electrical inhomogeneity between grain and GB in CCTO based ceramics [30,35]. Impedance spectroscopy is employed to characterize grain and GB properties. Typical impedance spectra of the samples under 393 K are plotted in Fig. 5(a) as an example. In this paper, complex resistivity is used in the impedance spectra to exclude the geometric effects. Owing to huge discrepancy between grain and GB, only one semi-

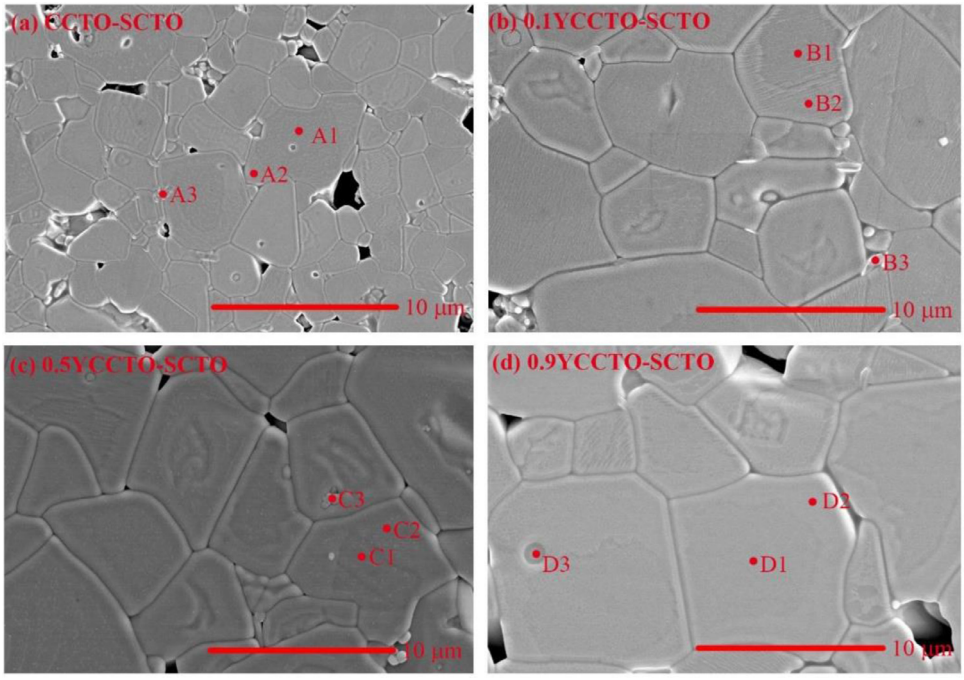

Fig. 3. Microstructures of 0 (a), 0.1 (b), 0.5 (c), 0.9 (d) YCCTO-SCTO composites.

Table 2
Ca/Sr distribution in various area of YCCTO-SCTO composite ceramic samples.

	CCTO-SCTO			0.1YCCTO-SCTO			0.5YCCTO-SCTO			0.9YCCTO-SCTO		
Element(wt%)	A1	A2	A3	B1	B2	B3	C1	C2	C3	D1	D2	D3
Ca	6.13	2.42	0.58	6.45	3.27	0.88	5.92	3.53	0.33	5.77	2.84	0.34
Sr	0.00	14.31	49.72	0.00	13.41	47.32	0.00	12.60	44.03	0.00	12.07	39.39
Y	0.00	0.00	0.00	0.30	0.99	4.11	0.36	1.86	14.78	2.83	4.77	20.90

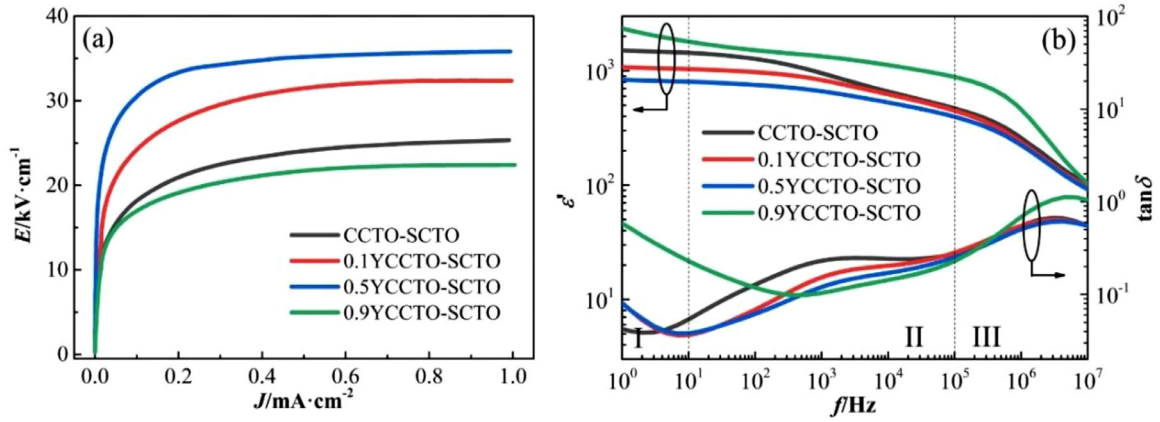

Fig. 4. Nonlinear current-voltage characteristics (a) and dielectric properties (b) of the composite ceramics.

circle representing for the GB can be observed [36]. As shown in Fig. 5(a), the curves fit well with Cole-Cole empirical relation, so that extrapolation is utilized to calculate the precise GB resistivity ρ_{gb} [36]. Moreover, Arrhenius equation is employed to describe the temperature dependence of GB resistivity:

$$\rho_{gb} = \rho_0 \exp(\frac{-E_{gb}}{kT}) \quad (3)$$

where E_{gb} stands for resistivity of GB and E_{gb} refers to grain/GB activation energy. Good linearity between $\ln E_{gb}$ and T^{-1} is observed in Fig. 5(b) so that E_{gb} and GB resistivity at room temperature is calculated by fitting the curves.

Fig. 6 summarizes the E_b, α, ρ_{gb} and E_{gb} of the composite samples, in which parameters of pristine CCTO ceramics are also listed in Fig. 6 for comparison [26,35,37,38]. Generally, improved E_{gb} and α are ascribed to the enhanced ρ_{gb} and E_{gb}, respectively [22,26,27,38–41]. Comparted to pristine CCTO samples, elevated ρ_{gb} and E_{gb} of the composite samples can be clearly observed in Fig. 6, which is accompanied by enhanced electrical properties. On the contrary, both E_{gb} and α of those composite samples differ greatly while their ρ_{gb} and E_{gb} are similar. In this perspective, it seems that E_{gb} and α have no significant correlation with GB properties for those composite samples, which is a contradiction based on former results.

Table 3
Breakdown field (E_{gb}), nonlinear coefficient (α), withstood voltage on single grain boundary (U_{gb}) of the YCCTO-SCTO composite ceramics.

Parameters	CCTO-SCTO	0.1YCCTO-SCTO	0.5YCCTO-SCTO	0.9YCCTO-SCTO
E_b (kV cm^{-1})	25.34	32.36	35.82	22.42
α	7.28	8.09	14.65	8.33
U_{gb} (V)	8.82	20.68	24.42	15.86

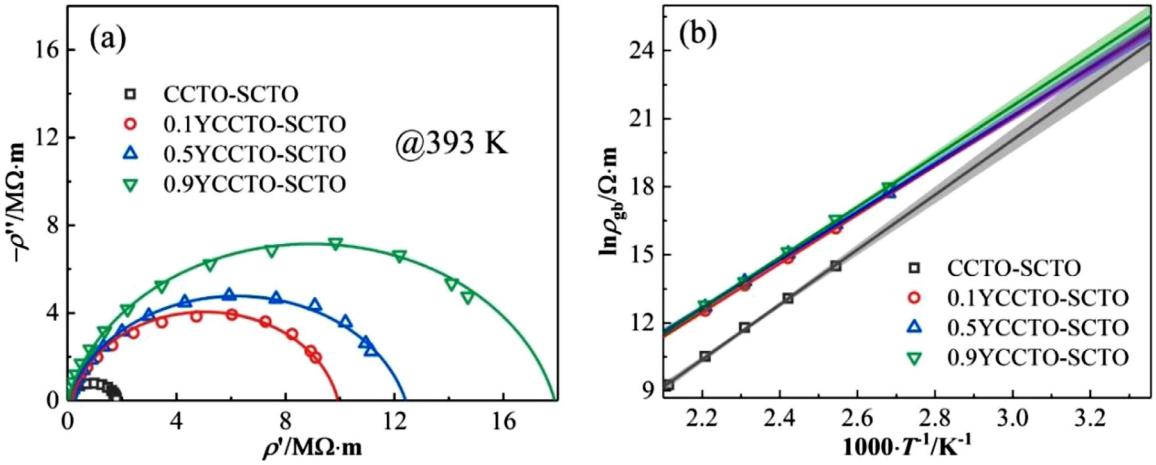

Fig. 5. Impedance spectra (a) and Arrhenius plots of resistivity of grain boundary (b) of the composite ceramic samples.

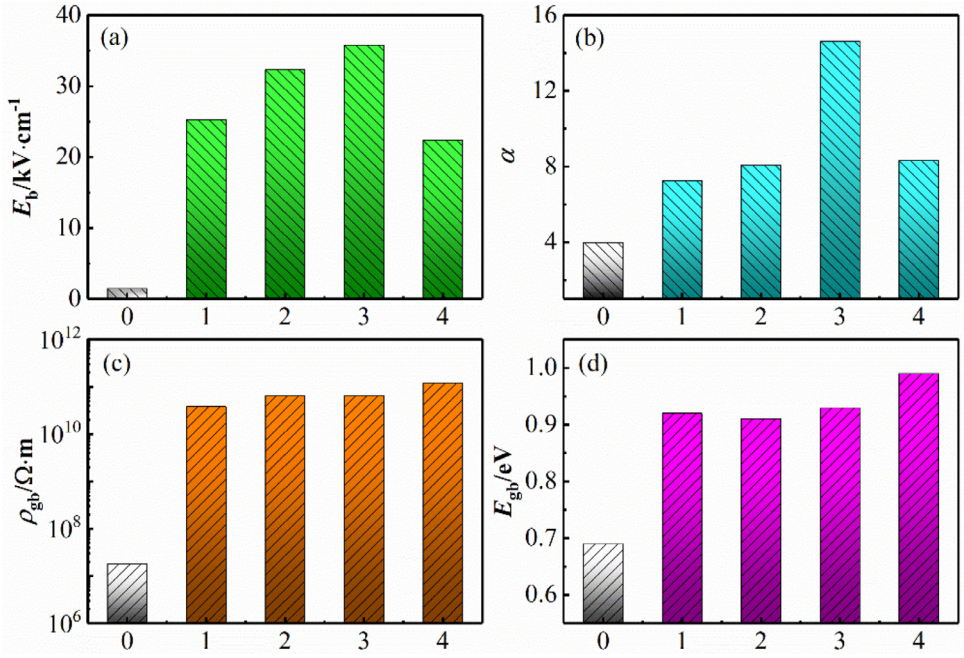

Fig. 6. Comparison of breakdown field (a), nonlinear coefficient (b), grain boundary resistivity (c) and its activation energy (d) of the composite samples to that of CCTO ceramics. (The numbers of 0–4 refer to CCTO, CCTO-SCTO, 0.1YCCTO-SCO, 0.5YCCTO-SCTO and 0.9YCTO-SCTO, respectively.).

In addition, it is remarkable that elevated E_b are detected in samples 0.1YCCTO-SCTO and 0.5YCCTO-SCTO with large average grain sizes. Generally, E_b is acknowledged as the voltage withstood by single GB times number of GBs on unit thickness:

$$\boldsymbol{U_{gb} = E_b d} \tag{4}$$

where U_{gb} is the voltage withstood by single GB and d is the average grain size shown in Fig. 3. Correlation between E_b and U_{gb} in previous reports are summarized in Fig. 7 [23,27,42–46]. U_{gb} of the most CCTO based samples remained 1.0–3.0 V, although E_b varied significantly from 1.2 to 32.2 kV cm^{-1}. It is indicated that U_{gb} of CCTO-based ceramics is a constant, which is similar to ZnO varistor ceramics. Notably, single GB of 0.5YCCTO-SCTO sample can endure more than 24 V, which is nearly 3 times of CCTO-SCTO sample and even 10 times of pristine CCTO samples. In other words, the significantly enhanced electrical properties in this work, reported for the first time, arise from optimized single GB rather than merely reducing the average grain size.

Therefore, it is reasonable to deduce that the commonly employed parameters of ρ_{gb} and E_{gb} are not enough to describe the optimization of GB in this work. It can be observed in Fig. 6 that both ρ_{gb} and E_{gb} are positively associated with withstood voltage

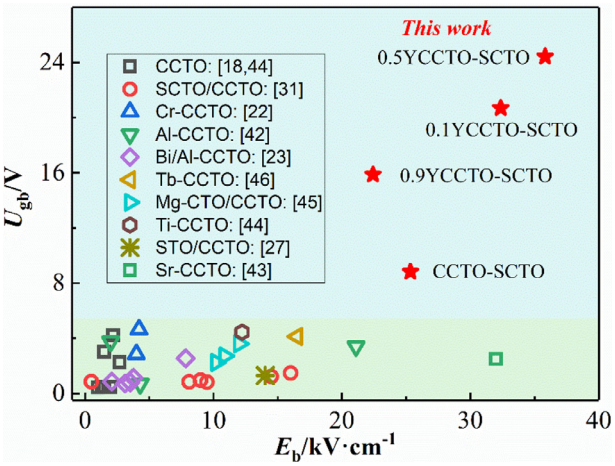

Fig. 7. Summary of the reported breakdown field and withstand voltage on single GB.

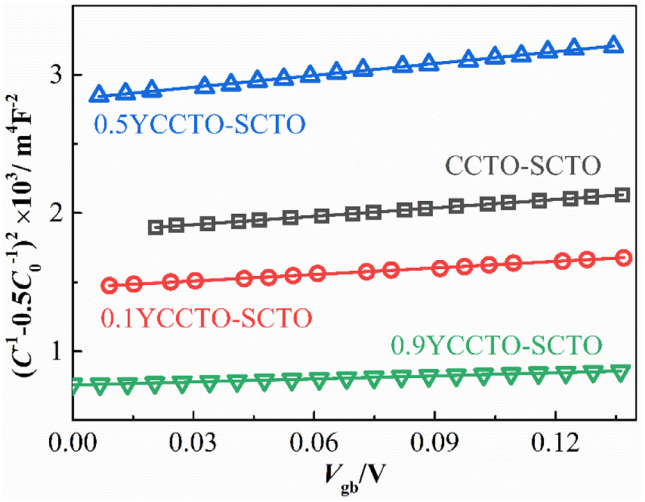

Fig. 8. Dependence of capacitance on voltage of the composite samples.

on single GB. Deeper understanding of Schottky barrier at GB from the level of point defects is of necessary.

3.4. Modification of interface state distribution

Initially, the capacitance-voltage (*C-V*) measurement was used to analyze the static barrier parameters. The interface between semiconducting grain and insulating GB can be ascribed as double Schottky barrier (DSB). When GB is applied DC bias, GB capacitance of unit area can be expressed as [36]:

$$\left(\frac{1}{C}-\frac{1}{2C_0}\right)^2=\frac{2}{e\varepsilon_0\varepsilon_r N_d}(\phi_0+V_{gb}) \tag{5}$$

where C and C_0 are GB capacitance with and without DC bias, respectively. V_{gb} is DC bias applied on the barrier, N_d is donor density, $\phi_0$is Schottky barrier height under zero voltage. The zero-bias interfacial charge density Q_{i0} is denoted as:

$$Q_{i0}=\sqrt{8e\phi_0\varepsilon_0\varepsilon_r N_d} \tag{6}$$

Fig. 8 is the dependence of $(1/C\text{-}0.5C_0)^2$ on voltage per GB (V_{gb}). Excellent linearity is observed between $(1/C\text{-}1/2C_0)^2$ and V_{gb}, indicating the nature of Schottky-type GB. Parameters of Schottky barrier including barrier height ϕ_0, donor density N_d and interfacial charge density Q_{i0} are concluded in Table 4. It is illustrated that ϕ_{b0} of the composite samples are similar to ~0.97 eV, although N_d and Q_{i0} differ greatly. The similar barrier heights calculated from *C-V* measurement are consistent with the GB resistivity activation energies E_{gb} calculated from impedance spectra.

Table 4
Donor density N_d, interface density N_s, Schottky barrier height under zero voltage ϕ_0 and depletion layer width of the YCCTO-SCTO composite ceramics.

Samples	ϕ_0 (eV)	N_d (10^{24} m^{-3})	Q_{i0}/e (10^{17} m^{-2})	w (nm)
CCTO-SCTO	0.94	8.39	5.29	31.53
0.1YCCTO-SCTO	0.96	10.79	6.05	28.03
0.5YCCTO-SCTO	0.98	6.20	4.65	37.51
0.9YCCTO-SCTO	1.01	24.23	9.32	19.23

It should be pointed out here that nonlinear *I-V* characteristics are dynamic responses of electron transportation. It depends on the ability of maintaining the barrier height under voltage, in addition to the initial height ϕ_0. In CCTO based ceramics, it well matches to heat-assistant field-emission model [18,41]:

$$J=J_0 e^{-\frac{e\phi_b+\xi}{kT}}\left(1-e^{-\frac{eV_{gb}}{kT}}\right) \tag{7}$$

where J is current density, J_0 is a constant and ϕ_b is barrier height. ζ is the bulk Fermi level, which is similar to the activation energy of grain resistance, and V_{gb} is voltage applied on single barrier. When the voltage is large enough, i.e., $eV_{gb}>>kT$, the current density is similar to:

$$J\approx J_0 e^{-\frac{e\phi_b+\xi}{kT}} \tag{8}$$

In this case, the current density is exponential related with the barrier height ($\ln J\propto\phi_b$). Therefore, nonlinear coefficient α can be understood as a parameter for characterizing the decreasing rate of barrier height under voltages by simply combining Eqs. (2) and (8). Higher α is achieved when the DSB could better maintain itself under applied voltages.

The DSB, as shown in Fig. 9(a), consists of negatively charged interfacial charge and positively charged depletion layers. Decrease of barrier height is closely related with electron filling of interface states [30,47]. Distortion of Schottky barrier, i.e., the reverse biased depletion layer expands while the forward biased depletion layer contracts, is formed when electric field is applied on it. Notably, the electrical field is mainly applied on the revere biased depletion layer. Increased positive charge caused by expansion of the reverse biased depletion layer is mainly compensated by electron filling of interface states to maintain electric neutrality. However, expansion of the reverse biased depletion layer can be only compensated by contraction of the forward biased depletion layer when interface states are fully filled. Rapidly decrease of barrier height is induced by significant contraction of the forward biased depletion. It is macroscopically shown as breakdown of the varistor ceramics. Similarly, high breakdown field E_b is achieved when the DSB could well maintain itself. Therefore, the nonlinear *I-V* properties of CCTO based ceramics depend significantly on the dynamics of electron filling in the interface states.

According to Blatter and Greuter's theory, relation between barrier height and applied voltage is expressed as [30,47]:

$$\phi_b=\frac{V_c}{4}\left(1-\frac{V_{gb}}{V_c}\right)^2 \tag{9}$$

where V_{gb} is the bias voltage applied on single GB. V_c is the critical voltage, which is defined as:

$$V_c=\frac{{Q_i}^2}{2eN_d\varepsilon_0\varepsilon_r} \tag{10}$$

where Q_i stands for interfacial charge density. When voltage is applied on DSB, interfacial charge increases so that decrease of barrier height is weakened. Barrier height under the applied voltage

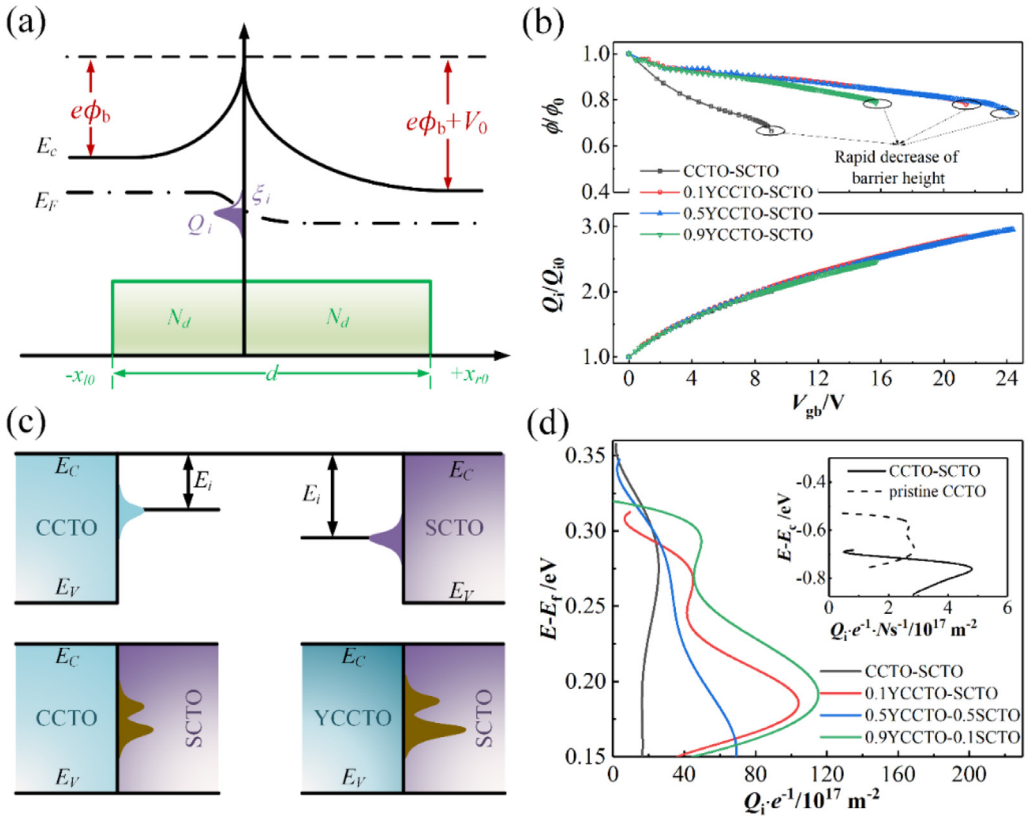

Fig. 9. Schematic of double Schottky barrier (a) and voltage dependence of barrier height and interfacial charge density of the composite ceramics (b). Schematic diagram of forming board and deep interface states in CCTO based composites (c) and calculated distribution of interface states of the composite samples (d).

can be easily obtained as $kT[ln(J_0/J)-\zeta]/e$, according to Eq. (8). The only left problem is to calculate $\ln J_0$. Fortunately, the current density could also be expressed as:

$$J = J_0 e^{-\frac{e\phi_{b0}-\beta\sqrt{E}}{kT}} \tag{11}$$

The value $\ln J_0$ is obtained by linearly fitting $\ln J \sim E^{1/2}$. According to Eq. (11), it is equation to the intercept of the curve.

Therefore, to quantitatively evaluate the velocity of barrier height descent and dynamics of electron filling in the interface states, two normalized parameters, ϕ/ϕ_0 (ϕ: Schottky barrier height, ϕ_0: zero-bias Schottky barrier height) and Q_i/Q_{i0} (Q_i: interfacial charge density, Q_i: zero-bias interfacial charge density), are proposed. Both the dependence of barrier height descent and interfacial charge density dynamics on the voltage applied on single DSB are calculated and plotted in Fig. 9(b). With the increase of applied voltage, barrier height slowly decreases in the initial process. Remarkably, barrier height dramatically decreases when the applied voltage reaches breakdown voltage, as marked by ellipses and current exponentially increases at this time. Interfacial charge density gradually increases and finally reaches to its maximum at breakdown voltage. Based on the assumption that interface states are fixed to the conduction band [47], distribution of interface states is calculated and plotted in Fig. 9(d). In addition, distribution of normalized interface states of pristine CCTO and CCTO-SCTO sample is plotted in the inset as a comparison. The discrepancy of interface state distribution resulted from the formation of heterogeneous interface, i.e., interface of Ca-G and Sr-G region characterized by EDS in Table 2.

Apparently, deeper interface states are developed in CCTO-SCTO composite ceramics compared to pristine CCTO ceramics. Since Schottky barrier height is pinned by interface states [30,47], formation of deeper level interface states results in higher barrier height. Therefore, deep interface states in CCTO-SCTO composite ceramics result in elevated barrier height of 0.97 eV compared to that of 0.65 eV in pristine CCTO ceramics as shown in Fig. 6. In addition, *Y* trends to separate at GB, which is also involved in forming interface states. As presented in Fig. 9(d), density of deep interface states increased after *Y* is doped into the samples. More electrons can be captured by interface states. Therefore, enhanced nonlinear properties are observed in *Y* doped composite sample, although their zero-bias barrier heights are similar. Specifically, broad distribution of interface states is formed in 0.5YCCTO–CCTO sample, where equal inhomogeneous YCCTO/SCTO junctions are formed. It was clearly presented by Blatter and Greuter that initial electron filling of interface states under zero bias is less for a broader distribution of interface states [47]. Therefore, more electrons can be filled when the voltage further increases. In other words, broader distribution of interface states is beneficial for extending the voltage range where the barrier could maintain a high height. As a result, with a similar zero-bias barrier height, nonlinear coefficient and breakdown field of the samples could be further enhanced by broadening interface states. In this case, highest breakdown field of 35.8 kV cm^{-1} and nonlinear coefficient of 14.6 are observed in 0.5YCCTO–CCTO samples.

4. Conclusion

The novel system of $Ca_{1-2x/3}YxCu3Ti4O12$-SrCu3Ti4O12 composite ceramics was prepared by the solid-state reaction method in this work. Extremely high breakdown field of more than 30 kV cm−1 and nonlinear coefficient of more than 14 were obtained in this composite ceramic system. Meanwhile, as the grain size remained more than 6 μm, the withstand voltage on single GB can reach up to 24 V, which is approximately 10 times than that of

common CCTO based ceramics. Since the Schottky barrier height and the GB resistance barely vary with the increasing *Y* concentration, the optimized varistor performance cannot be attributed to the elevated electrical heterogeneity between grains and GBs, i.e., IBLC model. Therefore, the nonlinear *I-V* properties of CCTO based ceramics are proposed to be related with dynamics of electron filling of the interface states. By a systematical analysis on the interface states, the excellent nonlinear properties can be ascribed to deeper and broader distribution of interface states, which points out a novel method to design CCTO based composite ceramics with high nonlinear performance.

Acknowledgments

This work was financially supported by the National Natural Science Foundation of China (No. 51937008) and the Science and Technology Project of State Grid Corporation of China (SGCC) (No. 5216A01600W3).

Supplementary materials

Supplementary material associated with this article can be found, in the online version, at doi:10.1016/j.jmst.2021.07.057.

References

[1] Y. Wang, W. Jie, C. Yang, X. Wei, J. Hao, Adv. Funct. Mater. 29 (2019) 1808118.
[2] F. Yan, Y. Shi, X. Zhou, K. Zhu, B. Shen, J. Zhai, Chem. Eng. J. 417 (2020) 127945.
[3] L. Zhang, Y. Pu, M. Chen, T. Wei, X. Peng, Chem. Eng. J. 383 (2020) 123154.
[4] A.P. Ramirez, M.A. Subramanian, M. Gardel, G. Blumberg, D. Li, T. Vogt, S.M. Shapiro, Solid State Commun. 115 (2000) 217–220.
[5] R. Schmidt, M.C. Stennett, N.C. Hyatt, J. Pokorny, J. Prado-Gonjal, M. Li, D.C. Sinclair, J. Eur. Ceram. Soc. 32 (2012) 3313–3323.
[6] M.A. Subramanian, A.W. Sleight, Solid State Sci. 4 (2002) 347–351.
[7] M. Ahmadipour, M.F. Ain, Z.A. Ahmad, Nano Micro Lett. 8 (2016) 291–311.
[8] N.T. Taylor, F.H. Davies, S.G. Davies, C.J. Price, S.P. Hepplestone, Adv. Mater. 31 (2019) 1904746.
[9] S.Y. Chung, I.D. Kim, S.J. Kang, Nat. Mater. 3 (2004) 774–778.
[10] M.A. Ramírez, P.R. Bueno, J.A. Varela, E. Longo, Appl. Phys. Lett. 89 (2006) 212102.
[11] M. Maleki Shahraki, S. Alipour, P. Mahmoudi, A. Karimi, Ceram. Int. 44 (2018) 20386–20390.
[12] Z. Tang, K. Wu, J. Li, S. Huang, J. Eur. Ceram. Soc. 40 (2020) 3437–3444.
[13] Z. Peng, J. Li, P. Liang, Z. Yang, X. Chao, J. Eur. Ceram. Soc. 37 (2017) 4637–4644.
[14] B. Cheng, Y. Lin, W. Deng, J. Cai, J. Lan, C. Nan, X. Xiao, J. He, J. Electroceram. 29 (2012) 250–253.
[15] T. Li, Z. Chen, F. Chang, J. Hao, J. Zhang, J. Alloys Compd. 484 (2009) 718–722.
[16] L. Liu, L. Fang, Y. Huang, Y. Li, D. Shi, S. Zheng, S. Wu, C. Hu, J. Appl. Phys. 110 (2011) 094101.
[17] J. Yuan, Y. Lin, H. Lu, B. Cheng, C. Nan, J. Am. Ceram. Soc. 94 (2011) 1966–1969.
[18] T. Li, Y. Sun, H.Y. Dai, D.W. Liu, J. Chen, R.Z. Xue, Z.Q. Chen, J. Alloys Compd. 829 (2020) 154595.
[19] L. Liu, H. Fan, P. Fang, X. Chen, Mater. Res. Bull. 43 (2008) 1800–1807.
[20] P. Mao, J. Wang, L. Zhang, S. Liu, Y. Zhao, Q. Sun, J. Mater. Sci. Mater. Electron. 30 (2019) 13401–13411.
[21] S. Pongpaiboonkul, T.M. Daniels, J.H. Hodak, A. Wisitsoraat, S.K. Hodak, Appl. Surf. Sci. 540 (2021) 148373.
[22] E.C. Grzebielucka, J.F.H. Leandro Monteiro, E.C.F. de Souza, C.P. Ferreira Borges, A.V.C. de Andrade, E. Cordoncillo, H. Beltrán-Mir, S.R.M. Antunes, J. Mater. Sci. Technol. 41 (2020) 12–20.
[23] L. Ren, L. Yang, C. Xu, X. Zhao, R. Liao, J. Alloys Compd. 768 (2018) 652–658.
[24] Z. Tang, K. Wu, J. Li, S. Huang, Ceram. Int. 46 (2020) 16949–16955.
[25] J. Boonlakhorn, N. Chanlek, P. Thongbai, P. Srepusharawoot, J. Phys. Chem. C 124 (2020) 20682–20692.
[26] J. Li, K. Wu, R. Jia, L. Hou, L. Gao, S. Li, Mater. Des. 92 (2016) 546–551.
[27] P. Mao, J. Wang, L. He, L. Zhang, A. Annadi, F. Kang, Q. Sun, Z. Wang, H. Gong, ACS Appl. Mater. Interfaces 12 (2020) 48781–48793.
[28] D.C. Sinclair, T.B. Adams, F.D. Morrison, A.R. West, Appl. Phys. Lett. 80 (2002) 2153–2155.
[29] A. Cho, C.S. Han, M. Kang, W. Choi, J. Lee, J. Jeon, S. Yu, Y.S. Jung, Y.S. Cho, ACS Appl. Mater. Interfaces 10 (2018) 16203–16209.
[30] K. Wu, Y. Wang, Z. Hou, S. Li, J. Li, Z. Tang, Y. Lin, J. Phys. D Appl. Phys. 54 (2021) 045301.
[31] Z. Tang, Y. Huang, K. Wu, J. Li, J. Eur. Ceram. Soc. 38 (2018) 1569–1575.
[32] J. Boonlakhorn, P. Kidkhunthod, B. Putasaeng, T. Yamwong, P. Thongbai, S. Maensiri, J. Mater. Sci. Mater. Electron. 26 (2015) 2329–2337.
[33] L. Tang, F. Xue, P. Guo, Z. Xin, Z. Luo, W. Li, Ceram. Int. 44 (2018) 18535–18540.
[34] D. Mori, M. Shimoi, Y. Kato, T. Katsumata, K. Hiraki, T. Takahashi, Y. Inaguma, Ferroelectrics 414 (2011) 180–189.
[35] K. Wu, Y. Huang, J. Li, S. Li, Appl. Phys. Lett. 111 (2017) 042902.
[36] Y. Huang, K. Wu, Z. Xing, C. Zhang, X. Hu, P. Guo, J. Zhang, J. Li, J. Appl. Phys. 125 (2019) 084103.
[37] K. Wu, Y. Huang, L. Hou, Z. Tang, J. Li, S. Li, J. Mater. Sci. Mater. Electron. 29 (2018) 4488–4494.
[38] P. Mao, J. Wang, S. Liu, L. Zhang, Y. Zhao, K. Wu, Z. Wang, J. Li, Ceram. Int. 45 (2019) 15082–15090.
[39] J. Wang, Z. Lu, T. Deng, C. Zhong, Z. Chen, J. Eur. Ceram. Soc. 38 (2018) 3505–3511.
[40] P. Saengvong, J. Boonlakhorn, N. Chanlek, B. Putasaeng, P. Thongbai, Ceram. Int. 46 (2020) 9780–9785.
[41] J. Jumpatam, B. Putasaeng, N. Chanlek, J. Boonlakhorn, P. Thongbai, N. Phromviyo, P. Chindaprasirt, Mater. Res. Bull. 133 (2021) 111043.
[42] R. Jia, X. Zhao, J. Li, X. Tang, Mater. Sci. Eng. B 185 (2014) 79–85.
[43] A.A. Felix, L.A. Saska, V.D.N. Bezzon, M. Cilense, Ceram. Int. 45 (2019) 14305–14311.
[44] K. Prompa, E. Swatsitang, C. Saiyasombat, T. Putjuso, Ceram. Int. 44 (2018) 13267–13277.
[45] J. Jumpatam, B. Putasaeng, T. Yamwong, P. Thongbai, S. Maensiri, J. Eur. Ceram. Soc. 34 (2014) 2941–2950.
[46] P. Thongbai, J. Boonlakhorn, B. Putasaeng, T. Yamwong, S. Maensiri, J. Am. Ceram. Soc. 96 (2013) 379–381.
[47] G. Blatter, F. Greuter, Phys. Rev. B 33 (1986) 3952–3966.